Journal of Alloys and Compounds 890 (2021) 161923

Contents lists available at ScienceDirect

Journal of Alloys and Compounds

journal homepage: www.elsevier.com/locate/jalcom

Chemical vapour deposited ZnO nanowires for detecting ethanol and NO_2

Eric Navarrete[a], Frank Güell[b], Paulina R. Martínez-Alanis[c], Eduard Llobet[a,*]

[a] MINOS-EMaS, Universitat Rovira i Virgili, Avda. Països Catalans, 26, 43007 Tarragona, Spain
[b] ENFOCAT-IN^{2}UB, Universitat de Barcelona, C/Martí i Franquès 1, 08028 Barcelona, Catalunya, Spain
[c] Universitat de Barcelona, Dept. de Química Inorgànica i Orgànica, C/Martí i Franquès 1, 08028 Barcelona, Catalunya, Spain

ARTICLE INFO

Article history:
Received 25 May 2021
Received in revised form 4 August 2021
Accepted 6 September 2021
Available online 11 September 2021

Keywords:
ZnO
Nanowires
Gas sensing
Chemical vapor deposition
Ethanol
NO_2

ABSTRACT

Randomly oriented ZnO nanowires were grown directly onto alumina substrates having platinum interdigitated screen-printed electrodes via the chemical vapor deposition method using Au as catalyst. Three different Au film thicknesses (i.e., 3, 6 or 12 nm) were used in the growth of nanowires, and their gas sensing properties were studied for ethanol and NO_2 as reducing and oxidizing species, respectively. ZnO nanowires grown employing the 6 nm thick layers were the less defective and showed the most stable, repeatable gas sensing properties. Despite ZnO nanowires grown employing the thickest Au layers reached the highest responses under dry conditions, ZnO nanowires grown using the thinnest Au film were more resilient at detecting NO_2 in the presence of ambient moisture. The gas sensing results are discussed in light of the defects and the presence of Au impurities in the ZnO nanowires, as revealed by the characterization techniques used, such as X-ray diffraction, field-emission scanning electron microscopy, X-ray photoelectron spectroscopy and photoluminescence spectroscopy. Promising results were obtained by the implementation of ZnO NWs directly grown over alumina substrates for the detection of ethanol and NO_2, substantially ameliorating our previously reported results.

1. Introduction

ZnO has attracted interest for its outstanding properties, such as transparency, piezoelectricity, and conductivity [1]. To exploit these properties ZnO has been grown as a film by e-beam evaporation [2], DC and RF sputtering [3,4], pulsed laser deposition [5], sol-gel [6], or as nanostructures such as nanoflowers, nanowires and nanorods [7–9]. The semiconducting nature of ZnO stimulated new perspectives in research on new electronic devices, such as memristors [10,11] and in a wide range of fields as the ceramic industry [12], photocatalysis [13,14], piezotronics [15], electroluminescence [16,17] and gas sensing [18,19]. Zinc oxide was one of the first metal oxides to be studied for developing chemoresistive sensors. Already in 1978, Okuma et al. developed a sensor for detecting gases from liquid petroleum employing ZnO films [20]. During the early eighties, different authors reported the use of ZnO, either pure or loaded with catalytic metals, for sensing ethanol, carbon monoxide, methane, hydrogen sulphide, hydrogen, ammonia or nitrogen oxides [21–26]. All these gaseous species are important targets for inexpensive gas sensors because they are relevant to many applications such as home safety, livestock building management or air quality monitoring. Even though SnO_2 has become the most researched and the most successful material in commercial chemoresistive sensors, ZnO has retained its research appeal over the years. This interest in ZnO as a gas sensitive material has increased even further in the last years, especially with the study of nanostructured materials such as nanorods [27], nanowires (NWs) [28,29], nanospheres [30], nanotetrapods [31,32] or nanoflowers [33]. Gas-sensitive ZnO nanomaterials have been synthesized using a wide range of methodologies, which include hydrothermal and solvothermal methods [34–36], electrospinning [37–39] or chemical vapor deposition (CVD) [40–45], only to cite a few. Table 1 gives an overview of the most relevant results achieved in the detection of ethanol or nitrogen dioxide (NO_2) employing chemoresistors of pure ZnO nanomaterials in the last 16 years. The gas sensing properties of ZnO nanomaterials heavily depend on their dimensions, structure and chemical composition. While increasing the surface to volume ratio in nanomaterials has been used to enhance sensitivity, the crystalline facets actually exposed to the chemical environment, together with the presence of defects such as zinc interstitials (Zn_i), zinc vacancies (V_{Zn}), oxygen interstitials (O_i), oxygen vacancies (V_O), and its recombination, play a major role in the reactivity and potential selectivity of ZnO nanomaterials [28,29,34]. The catalysed [28] and

* Corresponding author.
E-mail addresses: frank.guell@ub.edu (F. Güell), paulina.martinez@ub.edu (P.R. Martínez-Alanis), eduard.llobet@urv.cat (E. Llobet).

https://doi.org/10.1016/j.jallcom.2021.161923
0925-8388/

Table 1
Summary of results reported previously employing sensors based on ZnO NWs.

ZnO structure	Synthesis/coating method	Operating temperature	Gas/Range (ppm)	Response		Ref.
Thin film	Spin coating	200 °C	NO_2/1	[c]21.8		[46]
NWs	CTAB assisted Hydrothermal	400 °C	NO_2/40	[c]206		[47]
NWs	Hydrothermal	350 °C	NO_2/1	[c]1.8		[48]
NWs	Thermal evaporation	[a]NA	Ethanol/1000	42%		[49]
Thin film NWs	Dip-coating	375 °C	Ethanol/100	[b]68		[50]
A-NWs	VLS	250 °C	Ethanol/500	[b]4.3	[28]	
C-NWs			NO_2/100	[c]5.8		
NWs	VLS	200 °C	Ethanol/20	[b]9.2	This work	
		250 °C	NO_2/1	[c]51		

[a] NA. Not Available.
[b] (R_{air}/R_{gas}).
[c] (R_{gas}/R_{air}).

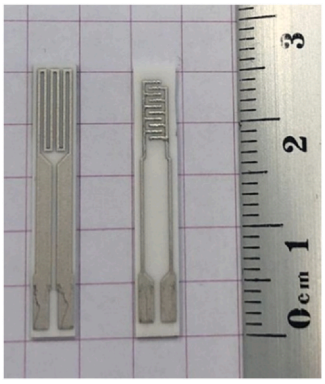

Fig. 1. Commercial alumina substrates. Left; Substrate back-face corresponding to the Pt heather. Right, front-face corresponding to the interdigitated Pt-electrodes. The interdigitated area comprises an effective area of approximately $3 \times 6\ mm^2$. Electrode fingers are 2 mm long, 300 µm wide and the gap between fingers is 300 µm.

self-catalysed [43] CVD method has been reported useful for growing single crystalline ZnO NWs. In Ref. [28], a catalysed CVD technique was employed for growing ZnO NWs on sapphire substrates that had different crystallographic orientations. The good match between the lattice parameter of ZnO and that of sapphire enabled the growth of ZnO NWs according to the different crystallographic orientations of the sapphire substrate. As a result, NWs grew vertically aligned or titled (with well-defined angles) to the substrate. Photoluminescence (PL) studies unveiled that ZnO NWs with different orientations had a different number and nature of defects (e.g. surface or deep-level defects), which affected the gas sensing properties.

In this paper, we report the direct growth of ZnO NWs on commercially available alumina substrates having screen-printed, platinum interdigitated electrodes and a heating meander. This direct assembly of the gas-sensitive nanomaterial on the alumina substrate eases the sensor fabrication process, avoiding the need for transferring the ZnO NWs from the growth substrate onto the application substrate. It also enables achieving good and stable contacts between the NWs and the electrodes. ZnO NWs were synthesized via a catalysed CVD process that results in a vapour-liquid-solid (VLS) growth mechanism. Gold layers of three different thicknesses were sputter-deposited over the bare alumina electrodes. Typically, in the CVD method the deposited Au catalyst layer is heated until to form drops of liquid Au over the substrate. Finally, the nucleation and growth of solid ZnO NWs occur due to supersaturation of the liquid Au droplets with Zn, O, and ZnO. The CVD grown ZnO nanowires completely cover the electrode area and bridge the interdigitated electrode gaps via multiple nanowire to nanowire contacts (given their disordered orientation). ZnO nanowires grow both on alumina and on the Pt screen-printed interdigitated electrodes, which ensures excellent adherence to the substrate and very reliable ZnO-electrode contacts. This is often not the case when nanomaterials need to be transferred from a growth substrate to their application substrate. For example, when nanomaterials are suspended in solvent solution and drop casted or spray coated over the electrode area of the application substrate, followed by solvent evaporation. The ZnO NWs density, composition, and defects are related to the Au catalyst thickness as revealed by the characterization techniques X-ray diffraction (XRD), field-emission scanning electron microscopy (FESEM), chemical mapping, X-ray photoelectron spectroscopy (XPS) and room-temperature PL. These differences are correlated with the observed gas sensing properties and a sensing mechanism is discussed.

2. Materials and methods

2.1. Au-catalyst deposition

Au thin films with various nominal thicknesses of 3, 6 and 12 nm were deposited by sputtering over the electrode area ($5 \times 5\ mm^2$) of alumina substrates. Ceramic substrates were commercially available Rubalit 708 by Ceram Tech GmBH, Plochingen, Germany, with a medium grain size of 3–5 µm and a typical surface roughness of 0.35 µm (Fig. 1). These substrates are sold with Pt, screen printed interdigitated electrodes (front) and heating resistor (back).

2.2. Synthesis of ZnO NWs

To synthesize ZnO NWs via VLS it is important to decompose the ZnO powder precursor into Zn^{2+} and O^{2-}, which occurs at high temperature (1350 °C). In order to reduce this temperature, the ZnO powder is usually mixed with graphite (C) powder, and the decomposition takes place at around 900 °C. At 900 °C, C reduces ZnO into Zn or Zn sub oxides, and the catalyst, which is Au in our case, rearranges as spherical nanoparticles (NPs). When Zn vapor arrives to the substrate it forms an alloy with those Au NPs. ZnO powder was mixed with C powder at 1:1 mol ratio and the synthesis was carried out in a horizontal quartz tube placed in a CVD furnace. The powder mixture and the substrate were placed in the centre of the furnace. Argon was used as an inert carrier gas and the furnace was heated from room temperature to 900 °C, the temperature rate was 60 °C/min, kept at 900 °C for 30 min (phase in which the growth takes place), and then naturally cooled down to room temperature. The powder mixture and the substrate were placed in the centre of the furnace. The powder to substrate distance was 1 cm. The argon gas flow was 400 sccm and the pressure inside the tube was maintained at 760 Torr during all the process. The different type of sensors fabricated were labelled as ZnO 3, ZnO 6 and ZnO 12, according to thickness of the Au catalyst films.

2.3. Structural, optical and compositional characterization

XRD measurements were made using a Bruker-AXS D8-Discover diffractometer equipped with parallel incident beam (Göbel mirror), vertical θ-θ goniometer, XYZ motorized stage and with a GADDS (General Area Diffraction System). Samples were placed directly on the sample holder for reflection analysis. An X-ray collimator system close-to-the-sample allows to analyse areas of 500 µm. The X-ray diffractometer was operated at 40 kV and 40 mA to generate Cu Kα radiation. The GADDS detector was a HI-STAR (multiwire proportional counter of 30 × 30 cm with a 1024 × 1024 pixel) placed at 15 cm from the sample. We collected one frame (2D XRD pattern) that covered at such distance a range from 20° up to 50° 2θ. The exposure time was 300 s per frame. The resulting images were 2θ integrated to obtain a 2θ conventional diffractogram. The morphology of the ZnO NWs and the chemical mapping were investigated by FESEM with a Hitachi H-4100FE. Room-temperature PL measurements were made using a chopped Kimmon IK Series He-Cd laser (325 nm and 40 mW). Fluorescence was dispersed with an Oriel Corner Stone 1/8 74000 monochromator, detected using a Hamamatsu H8259-02 with a socket assembly E717-500 photomultiplier, and amplified through a Stanford Research Systems SR830 DSP. A filter in 360 nm was used to stray light. All spectra were corrected for the response function of the setups. XPS measurements were performed in a PHI 5500 Multitechnique System equipped with a monochromatic X-ray radiation source of Al Kα (1486.6 eV) at 350 W. The sample was placed perpendicular to the analyser axis and calibrated using the $3d_{5/2}$ line of Ag with a full width at half maximum (FWHM) of 0.8 eV. The diameter circle of the analysed area was 0.8 mm. The resolution for the general and depth profile spectra were 187.5 eV of pass energy at 0.8 eV/step, and 23.5 eV of pass energy at 0.1 eV/step, respectively. All measurements were made in an ultra-high vacuum (UHV) chamber pressure ($5 \cdot 10^{-9}$ and $2 \cdot 10^{-8}$ Torr). The binding energies (BE) values were referred to the C 1s BE at 284.8 eV. Component analysis has been performed by constructive curve joint Shirley and Tougaard functions to determine the peak background, and the line shape of the curves was fitted with mixed Lorentzian-Gaussian at 10–30% ratio.

2.4. Gas sensing characterization

Similarly, to our previous work [28], the gas sensing tests were conducted in a laboratory environment where the sensor response and behaviour towards an oxidizing gas (NO_2 at 250, 500 and 1000 ppb) and a reducing vapor (ethanol at 5, 10 and 20 ppm) were studied. These concentrations were chosen because NO_2 is an atmospheric pollutant that should be detected in the tens to hundreds of ppb range and ethanol is released from cooking or can be found in exhaled breath of drinkers, typically in the ppm range. The different gas sensors were studied at the operating temperatures of 150, 200 and 250 °C. Gas sensing measurements consisted of continuously acquiring and recording the DC resistance of the sensors while they underwent repeated exposure and recovery cycles of either NO_2 or ethanol. The sensors were placed inside a Teflon, 21 ml volume, airtight gas chamber and their baseline resistance was stabilized under a continuous flow of pure dry air. Subsequently, the sensors undertook a sequence of cycles consisting of 60 min of synthetic dry air followed by a 15 min pulse of the target gas concentration followed by a 15 min of dry air as a cleaning step (enabling baseline recovery). A typical gas measurement cycle consisted of 15 min pulses of increasing gas concentrations, interleaved by 15 min exposures to dry air (i.e., cleaning steps). Measurements were conducted at atmospheric pressure. Gas flow was kept constant and equal to 100 ml/min throughout the whole measurement process, which enabled renovating completely the atmosphere of the chamber in about 13 s. Gas sensing cycles were repeated at least 5 times to check the reproducibility and study the variability among the responses. In addition to the gas sensing studies conducted in a background of dry air, measurements were conducted as well in a background of humidified air 50% relative humidity (R.H.), to better understand sensor behaviour when ambient moisture is present. Typically, the relative humidity found present inside building facilities is comprised between 40% and 60%, therefore, in an effort to reproduce such conditions and also to optimize efforts, the authors selected 50% R.H. as an average of such typical humidity levels in order to operate the sensors as close to real world conditions as possible. The dry gas stream is mixed with a calibrated amount of vapour water using an Environics Series 4040 system (Tolland, USA) to achieve the desired 50% R.H. prior to introducing the gas stream into the sensor test chamber. To verify that a constant relative humidity was kept throughout measurements, a commercial humidity and temperature sensor monitored the sensor gas chamber exhaust.

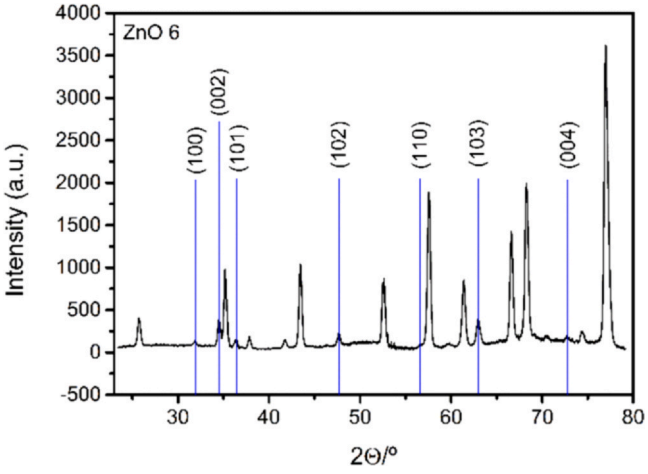

Fig. 2. XRD diffractogram for a typical ZnO 6 sample grown on top of an alumina substrate. The peaks with a blue line corresponds to the hexagonal ZnO pattern and the unlabelled peaks to the alumina substrate.

3. Results

3.1. Material characterization

Fig. 2 shows a typical XRD diffractogram of a ZnO sample. There were no significant differences in the diffractograms for the different ZnO samples grown (see Supporting information). All samples presented a hexagonal crystalline structure with a spatial group P63mc, in accordance with the ICDD card no. 36-1451. In contrast to our previously reported ZnO NWs on sapphire substrates [28], the ZnO NWs grown onto alumina substrates show a random orientation and a lack of predominantly exposed facets, as can be seen by the absence of preferential peaks in the XRD pattern. Typically, the roughness of the substrate used for the ZnO NW growth by CVD strongly influenced the distribution and orientation of the NWs over the surface. The non-labelled peaks in the diffractogram in Fig. 2, correspond to the alumina (ICDD card no. 46-1212) substrate where ZnO NWs are grown. The growth of randomly oriented mats of ZnO NWs could be anticipated as the alumina substrate (ceramic Rubalit 708) is characterized by a medium grain size of 3–5 µm and a typical surface roughness of 0.35 µm.

Fig. 3 shows typical FESEM micrographs for the three different types of samples grown and Fig. 4 shows the NWs at higher magnification. According to the XRD results these micrographs show a randomly oriented distribution of ZnO NWs over the alumina substrates in the three samples. As explained before, the granular, rough surface of the alumina substrate and the lattice mismatch existing

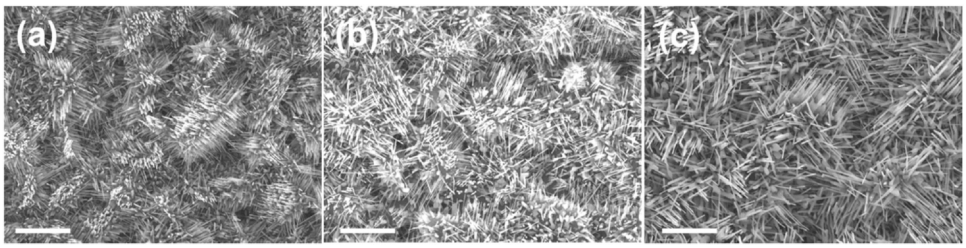

Fig. 3. FESEM images of the 3 different types of samples. ZnO 3 (a), ZnO 6 (b) and ZnO 12 (c). All scale bars are 3 µm.

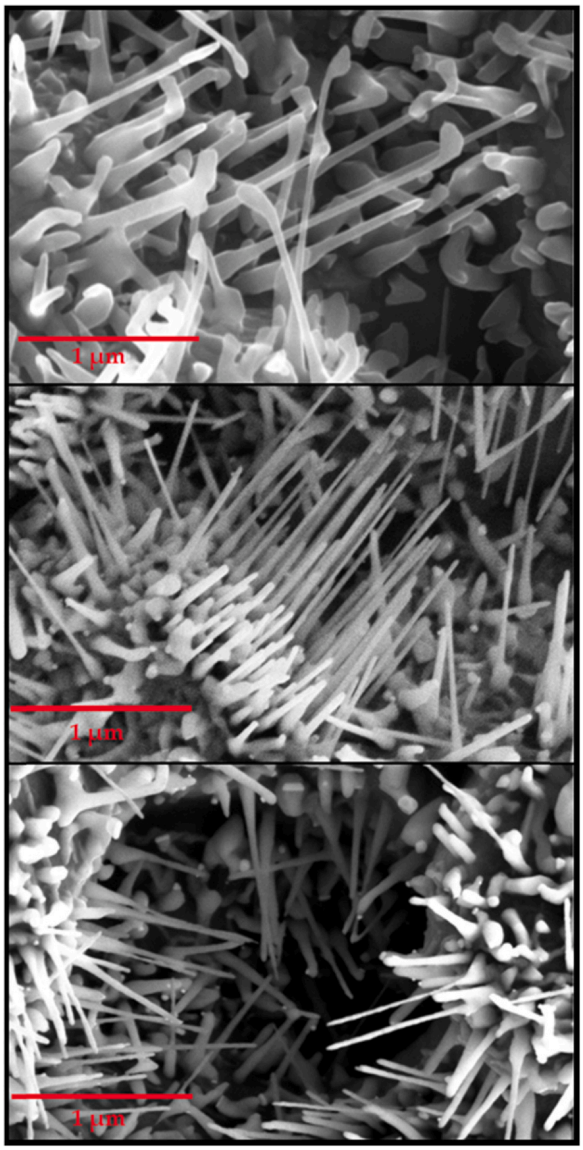

Fig. 4. FESEM micrographs obtained from the surface of the 3 different types of samples. ZnO 3 (upper panel), ZnO 6 (middle panel) and ZnO 12 (lower panel).

between hexagonal ZnO and α-Al_2O_3 promotes a randomly oriented growth of ZnO NWs [51]. The density, length, and diameter of the NWs varied among the different samples. In ZnO 3 samples, the average length of ZnO NWs was found to be about 1 µm while their average diameter was near 33 nm. NWs comprised a thicker zone (about 56 nm in diameter) in their close vicinity to the alumina substrate. In ZnO 6 samples, the average length of NWs was found to be near 600 nm with diameters near 34 nm on average. The thicker zone of NWs close to the alumina substrate is observed too. Finally,

Table 2
NW dimensions as a function of the Au catalyst thickness. Averaged values for 20 measurement points selected at random.

	Length (nm)	Near tip (nm)	Near substrate (nm)
ZnO 3	1000 ± 250	33 ± 5	56 ± 15
ZnO 6	600 ± 118	34 ± 6	65 ± 14
ZnO 12	500 ± 139	44 ± 10	83 ± 13

in ZnO 12 samples, ZnO NWs have an 83 nm diameter in their section close to the substrate to end up having a slightly thinner diameter of about 44 nm in their middle and terminal sections. The average length of NWs in ZnO 12 samples was found to be 500 nm, a similar value to the one of ZnO 6 samples yet displaying more irregular shapes. For the three types of samples grown (i.e., ZnO 3, ZnO 6 and ZnO 12) s, shorter and thicker wires co-exist with thinner and longer ones (see Fig. 4). However, Table 2 shows that thicker wires (especially at the region near the alumina substrate) are grown for thicker sputtered Au catalyst films.

The differences in diameter between the samples originated from the different thicknesses of the Au catalyst film sputtered onto the electrode area of the alumina substrates, are in good agreement with previously reported results [52]. For growing ZnO NWs the temperature is raised up to 900 °C. Then, Au liquid droplets are formed from the previously sputtered Au thin film, these droplets are the catalytic sites where the nucleation and growth of ZnO NWs take place and, as consequence, the diameter and density of the ZnO NWs depend on Au thickness [52]. Thinner Au films generate smaller sized Au droplets and thicker Au films lead to bigger Au droplets [53].

To understand better the chemical composition of the ZnO NWs present in the different samples, a chemical mapping was performed to study the composition and distribution of the Zn and Au atoms. The panels forming the left column in Fig. 5 were taken employing a backscattering detector to enhance changes in grayscale intensity according to the chemical elements present. Au NPs can be clearly distinguished apart from ZnO NWs in ZnO 6 and ZnO 12 samples, as these appear as bright spots (second and third rows in Fig. 5, respectively). The middle and right columns in Fig. 5 show a chemical mapping for Au (red) and Zn (yellow) atoms, respectively. No Au is visible in ZnO 3 samples (upper row, middle column in Fig. 5). In contrast, ZnO 6 samples are characterized by having Au NPs not only at the rod tips, but also quite homogeneously distributed along the NWs (second row, middle column in Fig. 5). Finally, the chemical mapping for a ZnO 12 samples, which is shown in the third row, middle and right columns in Fig. 5, indicates that Au NPs are located at the tips of the NWs, and not in their body, as it happened for ZnO 6 samples. A model was previously proposed for the Au-assisted growth of ZnO NWs, leading either to the presence of the Au-catalyst at the root (samples ZnO 3) (this is supported by a transversal cleavage analysis, please see the Supporting information), or at the tip (samples ZnO 6 and ZnO 12) of the ZnO NWs [54].

Fig. 6, summarizes the results obtained through the XPS analysis. The survey spectra for samples ZnO 3, ZnO 6 and ZnO 12 show the main signals corresponding to the Au 4*f*, Zn 3*p*, C 1*s*, O 1*s* and Zn 2*p*

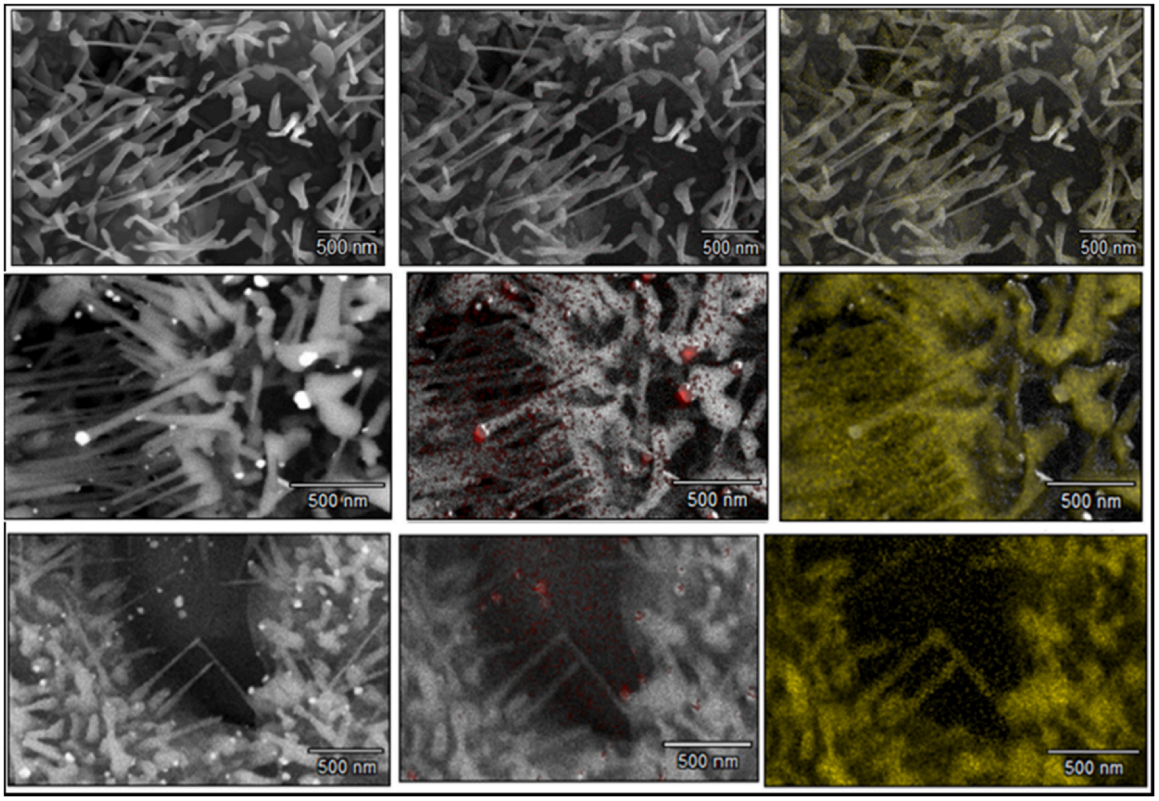

Fig. 5. FESEM images of an area selected at random in ZnO 3 (top row), ZnO 6 (middle row) and ZnO 12 (bottom row) samples. Left column panels correspond to backscattering images. Middle column panels show a chemical mapping in which Au atoms can be identified in red. Right column panels show a chemical mapping in which Zn atoms can be identified in yellow.

core levels, see Fig. 6(a). The analysis of the high-resolution spectra for the O 1s core level shows the contribution of the O-Zn, O═C, and OH species at around 530, 531.6 and 533. 5 eV BE, respectively, see Fig. 6(b) [55]. The analysis of the high-resolution spectra for the Au 4f core level is presented in Fig. 6(c). In this figure, the bands associated to the Au 4*f* and the Zn 3*p* core levels are overlapped, and the complex spectrum was deconvoluted in four components for samples ZnO 6 and ZnO 12 or three components for ZnO 3. The bands centred at around 83.2, 85.6, 88.5 and 91.5 eV BE being related to the Au 4 $f_{7/2}$ corel level of Au^0 and Au^+, and to the Zn $3p_{3/2}$ of the Zn-O and Zn-Au interaction, respectively, see Fig. 6(c) [56,57]. Note that the Au 4 $f_{7/2}$ core level at 83.2 eV BE is not observed for ZnO 3, see Fig. 6(c). This can be attributed to the kind of growth of the ZnO NWs in which the gold is encapsulated at the bottom for ZnO 3 samples. For the samples ZnO 6 and ZnO 12, the gold catalyst Au^0 appears at the tip of the ZnO NWs [58], and the Au 4 $f_{7/2}$ core level at 83.2 eV BE is observed, see Fig. 6(c). These results are in agreement with the FESEM images presented in Fig. 5, where the gold catalyst is observed at the tip of the ZnO NWs for samples ZnO 6 and ZnO 12, while no gold is visible for the ZnO 3 sample. The analysis of the high-resolution spectra in the region of C 1s core level band shows the contribution of four curves associated to the chemical bonds C–C, C═O, C–OH, O–C═O at around 284.6, 286.2, 287.8 and 288.7 eV BE, respectively, see Fig. 6(d). The main contribution corresponds to the chemical bond C–C associated to adsorbed carbon species. The analysis of the Zn 2p core level from the high-resolution spectra was done by the deconvolution of the curve in three components at around 1021.3, 1023.8 and 1024.7 eV BE, which correspond to the Zn–O, Zn–HCO_3 and Zn–OH chemical bonds, respectively, see Fig. 6(e). The main contribution corresponds to the Zn-O interaction in the wurtzite structure of ZnO.

The PL provides significant information about the crystal-quality of the samples by its implication in the optical properties of the material. Fig. 7 shows the room temperature PL spectra for ZnO 3, ZnO 6 and ZnO 12 samples. By pumping at 325 nm, we observed two emission bands, one strong emission in the UV at around 380 nm and a broader emission band in the visible range from 500 to 800 nm. The intensity of each spectrum was normalized to the intensity of the UV emission for relative comparison. The UV peak corresponds to the near band-edge emission, associated with exciton recombination processes [59], while the broad emission band observed in the visible range is generally attributed to defects [58]. The inset in Fig. 7 shows that the broad emission band in the visible has the maximum emission intensity at around 660 nm for the ZnO NWs grown using an Au-catalyst thin film of 3 nm, while for those grown using Au-catalyst thin films of 6 and 12 nm, the maximum is located near 630 nm. The origin of this broad visible emission band is still somehow controversial. Nevertheless, there is increasing consensus that it arises from radiative recombination processes related to defect/impurity complexes [58]. Although is not possible to unambiguously assign this band, its broadness can be related with the presence of defects with different characteristics: the 660 nm emission peak might correspond to O_i [60–67]. The 630 nm emission peak has been also observed in ZnO samples intentionally doped with Au impurities [68], and in Au NPs embedded in Au:ZnO composite films [69]. Indeed, this is in agreement with the results of the chemical mapping in Fig. 5, in which Au was clearly visible for ZnO 6 and ZnO 12 samples (Au was evenly distributed at the surface of ZnO NWs) but no Au was found in ZnO 3 samples. Furthermore, the non-displacement of the main peak at around 380 nm in the PL spectra for all the samples is in agreement with a shallow insertion of Au atoms in the crystal lattices of the ZnO NWs, which is also in agreement with the XRD results. In addition, the deep level emission

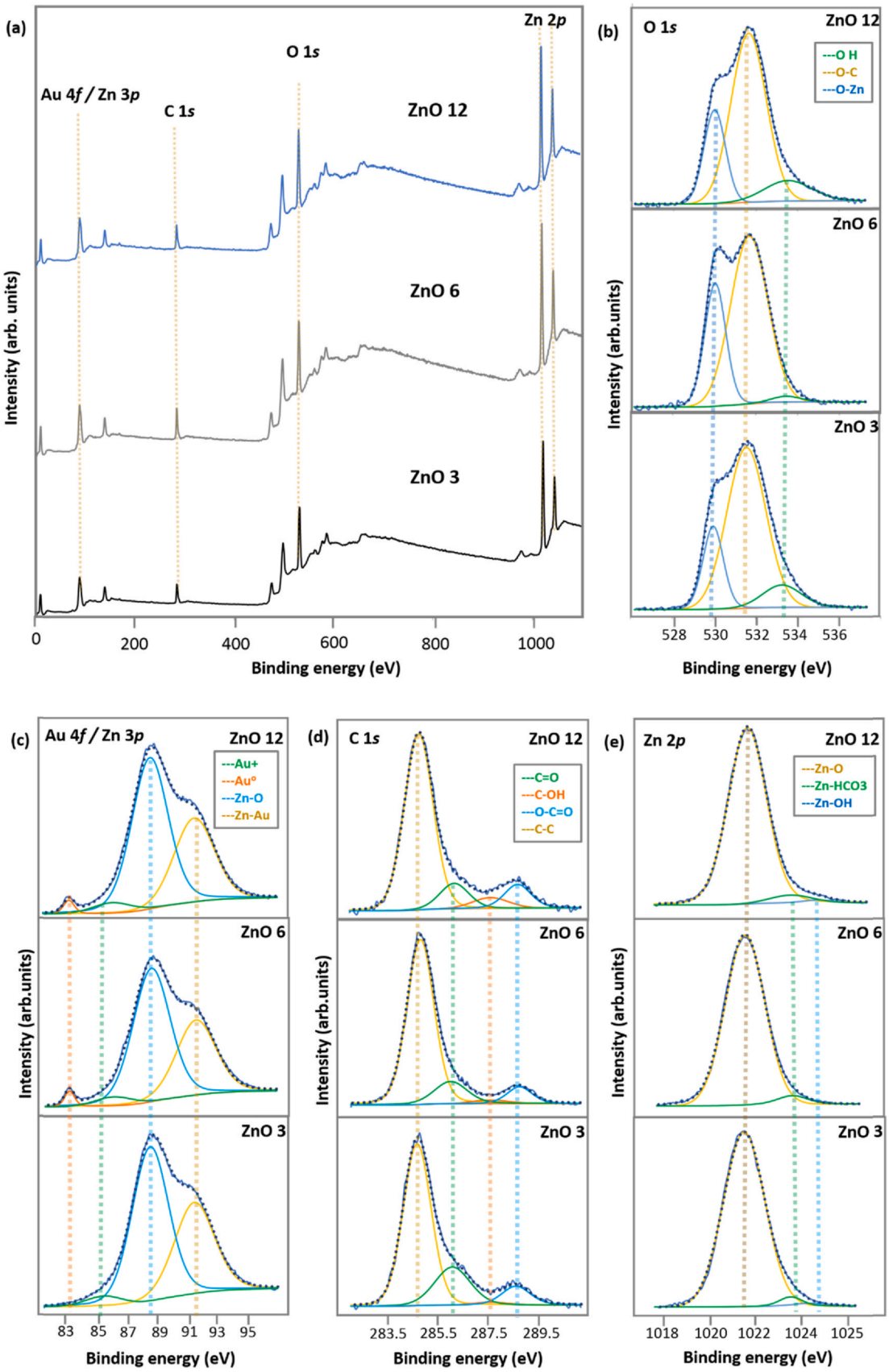

Fig. 6. Overview XPS spectra of samples ZnO 3, ZnO 6 and ZnO 12 (a). High-resolution XPS spectra for the O 1*s* (b), the Au 4*f* and Zn 3*p* (c), the C 1*s* (d) and the Zn 2*p* (e) core levels.

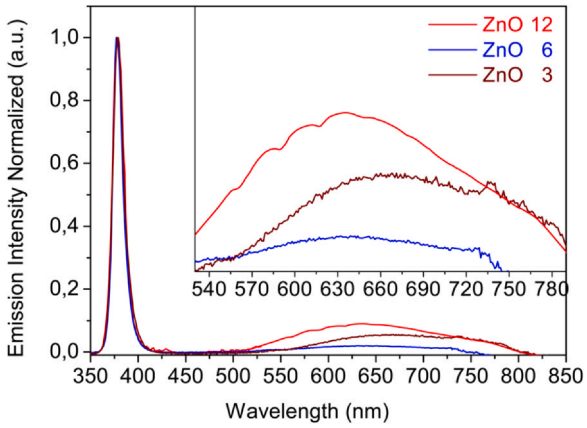

Fig. 7. Room-temperature PL emission spectra for the ZnO NWs grown over the electrode area of alumina substrates as a function of the thickness of the sputtered Au films.

to near-band-edge emission (DLE/NBE) ratio is an important criterion to evaluate the crystal quality between samples, i.e. the quantity of defects in the samples [70]. This ratio indicates that ZnO 12 samples had higher concentration of defects.

3.2. Gas sensing results

The gas sensing studies were conducted for sensors operated at 150, 200 and 250 °C in order to determine the best optimal working temperature at three different concentration levels for each target gas. For NO_2 the concentrations selected were 250, 500 and 1000 ppb and for ethanol the concentrations were 5, 10 and 20 ppm. The gas sensing studies were performed using dry air as carrier gas. Additionally, the calibrated gas bottles used dry air as balance gas. Under these conditions, the R.H. in the measurement rig was lower than 5% R.H. at 22 °C. Once the optimal operating temperatures had been identified, sensors were tested further under humid conditions (50% R.H. at 22 °C) to study the impact of ambient humidity on sensor performance. Sensor response was calculated as R_{air}/R_{gas} or R_{gas}/R_{air} when ethanol or NO_2 were measured, respectively. R_{air} is the baseline resistance of a sensor while under clean air and R_{gas} is the final value of sensor resistance under a given concentration of either ethanol or NO_2 at the end of a 15 min gas exposure. In Fig. 8 the evolution of sensor resistance for successive response and recovery cycles towards ethanol and NO_2 can be observed for the different sensor types operated at 250 °C. The resistance of the sensors exposed to ethanol (a reducing vapour) suffered a decrease in their resistance value, and the same sensors exposed to NO_2 (an oxidizing gas) suffered an increase in their resistance, as it could be expected for an *n*-type material such as ZnO. The different sensors showed a quite stable baseline resistance over the whole duration of response and recovery tests. The responses obtained for the two species measured were highly reproducible, especially for ZnO 6, which also showed the most stable baseline.

Furthermore, the T90 response time corresponds to the required amount of time to reach 90% of the maximum response value recorded. Additionally, if the exposure to a given species results in a resistance change ΔR, the T10 recovery time, corresponds to the time needed for sensor resistance to change from its final exposure value (i.e. baseline resistance ± ΔR) to the baseline resistance ± 0.1ΔR. Positive (negative) sign is for an exposure to an oxidizing (reducing) species. These values were calculated and are summarized in Table 3.

In Tonezzer et al. [71] report the response and recovery times for different types of NW gas sensors. In particular, they show that devices employing multiple NWs are characterised by significantly higher response and recovery times than those found in single NW

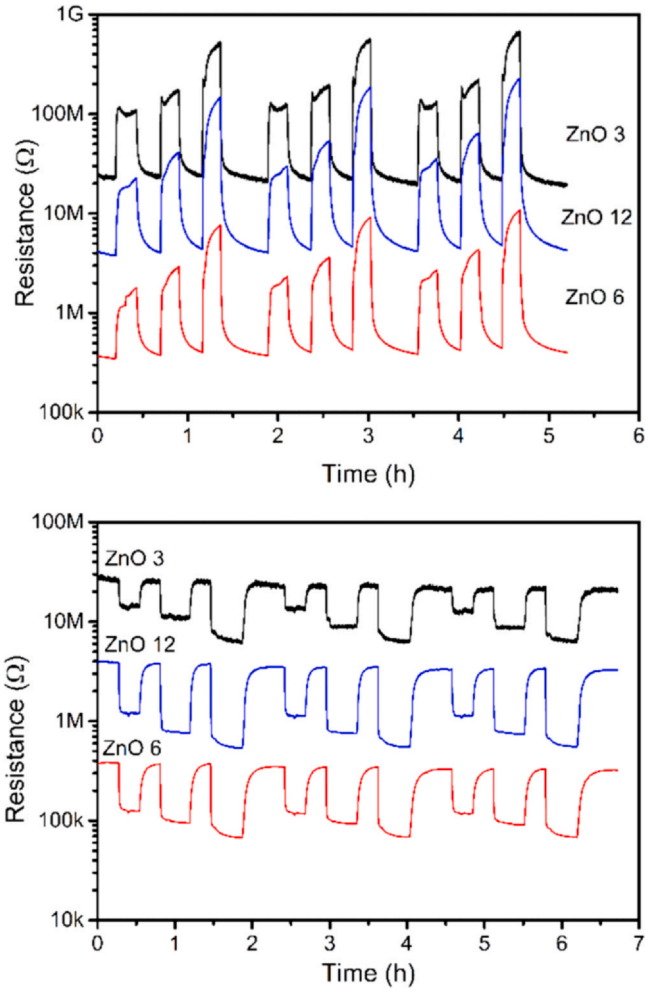

Fig. 8. Resistance behaviour for the three types of gas sensors studied to response and recovery cycles of increasing concentrations of NO_2 (upper panel) and ethanol (lower panel). Sensors were operated at 250 °C.

Table 3
Response (T90) and recovery (T10) times averaged for each gas at the maximum concentration analysed while sensors were operated at their optimal working temperatures.

Gas	Response time T90 (s)	Recovery time T10 (s)
Ethanol (20 ppm)	490 ± 27	566 ± 17
NO_2 (1 ppm)	565 ± 17	908 ± 2

devices. Particularly, denser multiple NW films show the lowest response and recovery dynamics, ranging between 350 and 1000 s. This is the case for the different ZnO NWs tested here in which the slow diffusion of the target gases within the mat of randomly oriented NWs is affecting response and recovery dynamics. This could be ameliorated by increasing the flow rate during measurements or by using UV light to speed up the cleaning (i.e. desorption of adsorbed molecules) of the sensing surface.

It is well known that the response to gases of semiconductor NW materials increases when their diameter decreases [72]. Here the diameter of ZnO NWs varies within a narrow range for the different samples grown (see Table 2), so these differences in diameter should have only mild effects on gas response.

SEM was performed before and after the gas sensing characterization, which took over one month and no significant changes in morphology were observed. XPS results performed at the end of the

Table 4
Averaged sensor responses (R_{gas}/R_{air}) and their standard deviations when exposed to 1 ppm of NO_2 at different operating temperatures under dry air conditions.

T (°C)	ZnO 3	ZnO 3 StDev	ZnO 6	ZnO 6 StDev	ZnO 12	ZnO 12 StDev
150	6.46	0.36	2.48	0.05	3.14	0.10
200	16.69	0.64	5.01	0.19	5.60	0.24
250	36.26	6.86	25.00	1.77	51.01	5.90

gas sensing study also confirm the stability of the ZnO samples over the gas sensing tests.

3.2.1. NO_2 results

The sensors exposed to NO_2 showed an increase in response as their operating temperature was increased. For instance, the averaged sensor responses for 1 ppm of NO_2 when performing gas sensing experiments are summarized in Table 4. The increase in response with operating temperature varied among the different sensors, being ZnO 3 the material displaying the lowest change (6 -fold increase when temperature was raised from 150 to 250 °C) and being ZnO 12 the material that experienced the highest increase in response (16-fold). Despite not showing the highest response, ZnO 6 was the material that achieved the highest repeatability through all the gas-sensing measurements. The sensor calibration curves for NO_2 when sensors were operated at 250 °C are summarized in Fig. 9. The slope of the calibration curves (i.e. sensitivity to NO_2) increases for samples having a higher number of defects (as revealed by the PL analysis in the visible region). Interestingly, in our previous study we reported that c-plane ZnO NWs displayed a response of 5.8 for 100 ppm NO_2 at 250 °C [28], meanwhile in this paper in which the materials have been directly grown onto the alumina substrate, we report significantly higher sensor responses, at much lower gas concentrations. Previously reported results indicate that pure ZnO nanomaterials show an optimal operating temperature for detecting NO_2 that ranges between 200 and 300 °C [33,72]. Since too high an operating temperature has detrimental effects in the long-term stability of nanomaterial sensors and increases power consumption, 250 °C was the highest operating temperature considered here. A calibration curve showing the effect of operating temperature on NO_2 response can be found in the Supporting information.

After having determined experimentally 250 °C as the optimal working temperature for NO_2 detection, the impact of ambient humidity was studied. The gas sensing experiments were repeated at 250 °C and the gas flow was humidified to 50% R.H. before being introduced into the test chamber. The results obtained are shown in Fig. 10. When humidity was introduced in the system, the overall sensor responses were negatively impacted. In average, the decrease in sensor response observed for 1 ppm of NO_2 was near a factor of 2 for both ZnO 3 and ZnO 6 samples. However, the most humidity-affected material was ZnO 12 with a 4.5-fold decreased response. Interestingly, ZnO 3 displayed in this case the higher responses for NO_2 under humid conditions and it is worth pointing out that the response of this nanomaterial towards 250 and 500 ppb of NO_2 was barely affected by the presence of humidity. The important decrease in the response towards NO_2 for ZnO 12 could be attributed to its higher concentration of defects, as revealed by PL. A more defective NW matrix could let to a higher amount of water molecules getting adsorbed and thus lowering the number of available sites for the target gas to react. Indeed, for ZnO 12, the XPS analysis reveals that the relative importance of the peak related to hydroxyls associated to oxygen-defective areas is higher than in any other sample, which supports this sample showing a higher hydroxylation.

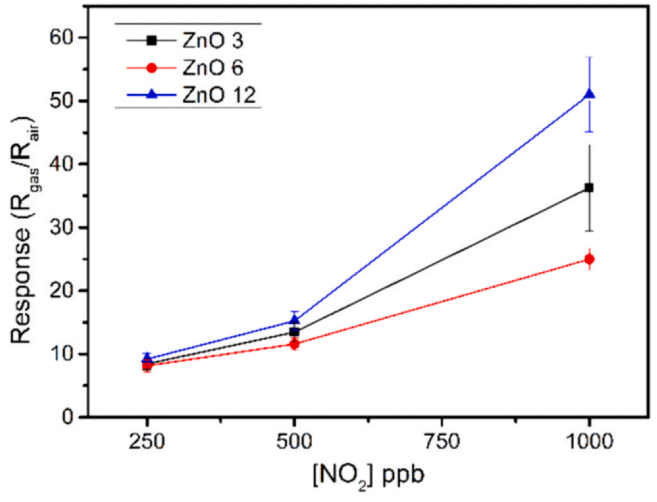

Fig. 9. Sensor calibration curves for NO_2. Sensors were operated at 250 °C under dry air conditions.

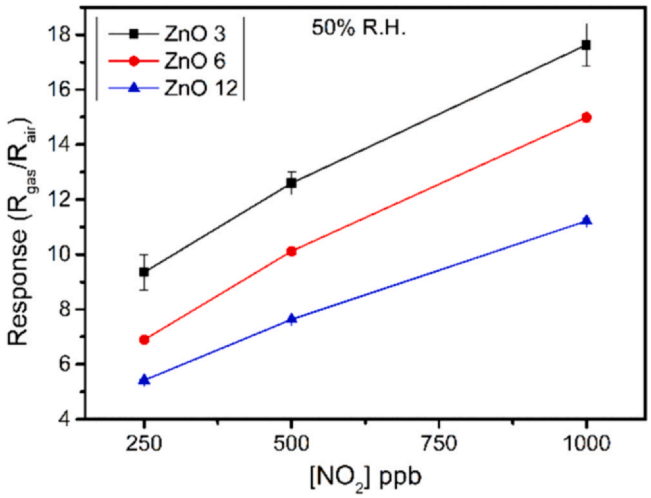

Fig. 10. Sensor calibration curves for NO_2. Sensors were operated at 250 °C under humidified air conditions (50% R.H.).

3.2.2. Ethanol results

Likewise, all materials were exposed to a sequence of ethanol cycles at different operating temperatures in order to identify the optimal working temperature. After testing different temperatures (150, 200 and 250 °C), it was found that the responses at 150 °C were very low. The highest response to ethanol was achieved when sensors were operated at 200 °C. However, as opposed to the results at 200 °C, responses were far more stable and reproducible when the sensors were operated at 250 °C. The diffusion of gas molecules within the highly porous films of ZnO wire mats during the response and recovery cycles is speeded up by operating temperature. At 200 °C, slower response and recovery dynamics result in poorer reproducibility of results for repeated detection and recovery cycles, as reaction by-products do not completely desorb and leave the gas sensitive material. A calibration curve showing the effect of operating temperature on ethanol response can be found in the Supporting information. Therefore, this temperature was selected as the most suitable operating temperature for detecting ethanol vapours because it implied a good trade-off between response intensity and measurement uncertainty. Table 5 summarizes the results obtained for each sensor at the maximum ethanol concentration tested.

Fig. 11 shows the calibration curves for ethanol vapours for the different sensor types operated at 250 °C. At such operating temperature, the higher the thickness of the Au catalyst layer was, the

Table 5
Averaged sensors responses (R_{air}/R_{gas}) and their standard deviations when exposed to 20 ppm of ethanol at different operating temperatures under dry air conditions.

T (°C)	ZnO 3	ZnO3 StDev	ZnO 6	ZnO6 StDev	ZnO 12	ZnO12 StDev
150	1.40	0.07	1.14	0.01	1.20	0.02
200	4.58	0.58	6.04	0.98	9.23	2.07
250	3.79	0.40	5.17	0.39	6.56	0.59

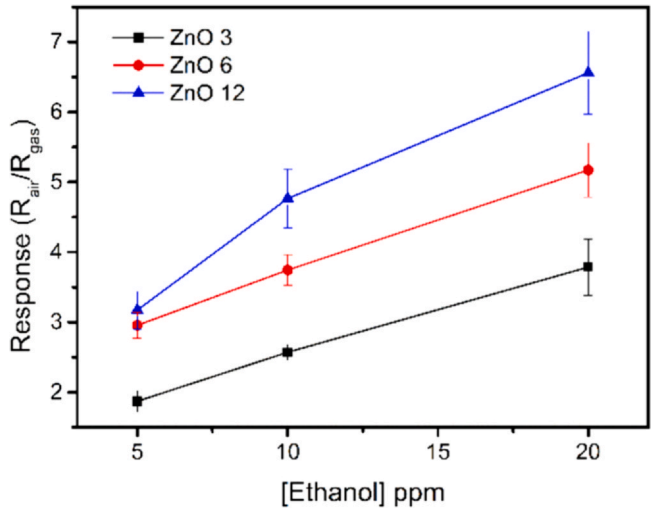

Fig. 11. Sensor calibration curves for ethanol vapours. Sensors were operated at 250 °C under dry air conditions.

higher the response towards ethanol was achieved. Furthermore, at the same operating temperature, the overall responsiveness of the different sensors towards ethanol is 7 times lower than that for NO_2. In a similar way to the case of NO_2, the response to ethanol reported here is significantly higher than the one reported previously. For example, the response of the ZnO 3 sample to ethanol 20 ppm reported here is like the response recorded towards ethanol 500 ppm for a-plane ZnO NWs, as reported in Ref. [28]. Once more, this is attributed to the better contact with the electrodes achieved when nanomaterials are grown directly over the alumina substrate.

Furthermore, the impact of ambient humidity was also studied for ethanol. The operating temperature chosen to perform the test was 250 °C and the relative humidity was, once more, set to 50% in order to make a better comparison between the behaviour of the different sensors in front of the two different gaseous species studied. Fig. 12 shows the results obtained for the sensors when tested for ethanol vapours under humid conditions. When ambient humidity was present, the response of ZnO 3 towards ethanol completely disappeared. In the case of ZnO 6 and ZnO 12, the response behaviour showed a similar pattern with the occurrence of a clear response saturation above 10 ppm of ethanol. In addition to this response saturation effect, ZnO 6 and ZnO 12 based sensors suffered a 2.4 and 3.5-fold decrease in their response to ethanol, respectively (for the two lowest concentrations tested). Considering the lack of ethanol response for ZnO 3, the decrease in response and response saturation observed for ZnO 6 and ZnO 12, it can be derived that the presence of ambient humidity has a higher impact in the detection of ethanol vapours than in NO_2 sensing.

4. Gas sensing mechanism

In sensors employing ZnO 3 as active material, the presence of Au catalyst was not observed in the chemical mapping nor in the XPS analysis. The results of the PL analysis reveal that ZnO 3 samples comprise a significant number of defects. Even though the maximum

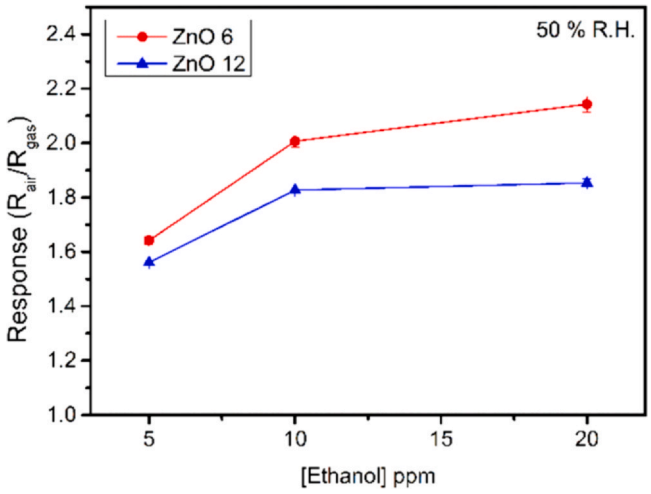

Fig. 12. Sensor calibration curves for ethanol. Sensors were operated at 250 °C under humidified air conditions (50% R.H.). The curve for ZnO 3 does not appear in this plot due to the lack of response observed under humid conditions for this material.

of the PL emission in the visible range is located at 660 nm, which is often attributed to the presence of O_i, the broadness of the emission band suggests that other defects such as Zn_i and V_O are present too [28]. Among these defects, those located at the surface generate sites for the adsorption of the NO_2 molecule, an electron acceptor that traps electrons from the conduction band of the ZnO semiconductor. In contrast, the ethanol molecule adsorbs and reacts with previously chemisorbed oxygen species, thus releasing electrons to the conduction band of ZnO. In addition, the process of oxygen ionosorption at the surface of ZnO is a thermally activated process. The activation energies were estimated for the different samples (see the Supporting information) and found to range between 0.7 eV (ZnO 12) to 0.76 eV (ZnO 6). These similar activation energies found throughout the different samples studied are indicative that the same surface processes of ionosorption of oxygen species occur. The chemical reactions formulae are shown from Eqs. (1)–(4):

$$NO_{2\ (gas)} \leftrightarrow NO_{2\ (ads)} \quad (1)$$

$$NO_{2\ (ads)} + e^- \rightarrow NO_{2\ (ads)}^- \quad (2)$$

$$O_{2\ (gas)} \leftrightarrow O_{2\ (ads)}^- \quad (3)$$

$$CH_3CH_2OH_{\ (gas)} + 3\ O_{2\ (ads)}^- \rightarrow 2\ CO_{2(gas)} + 3\ H_2O_{(gas)} + e^-flow \quad (4)$$

Additionally, the presence of catalyst metal particles (such as Au here) supported by ZnO NWs has been reported useful at sensitizing metal oxide nanomaterials in different ways. For example, by increasing the amount of adsorbed oxygen species on ZnO or by promoting the adsorption and reaction of target gases [72]. Here, the presence of Au NPs act as foreign receptors that enhance surface reactions and the adsorption of NO_2 resulting in enhanced response [73,74]. In the presence of ambient moisture, water molecules compete with ethanol for the adsorption sites and as the concentration of water is significantly higher than any of the concentrations tested for ethanol (50% R.H at 22 °C is circa 13,300 ppm of water), this explains why ZnO 3 samples in which no Au is present at their surface, show no response to ethanol under humid conditions. In contrast, the water-mediated adsorption of NO_2 at hydroxylated metal oxides has been reported [74], which explains why the response towards NO_2 is little affected by the presence of ambient moisture. Whenever humidity is present in the atmosphere it immediately adsorbs on sensor surface and this explains the differences found in the baseline resistance when the sensors are under

dry or under humid atmospheres. At 250 °C the absorption-desorption of water molecules and the occurrence of hydroxyl groups attached to the surface of metal oxides is still favoured. The presence of moisture shows competitive or synergistic effects for the adsorption of other species [75].

For sensors employing ZnO 6 and ZnO 12 samples, the presence of Au NPs was clearly shown in the chemical mapping and in the XPS analysis. The PL results indicate that ZnO 6 samples are the less defective among the different samples grown (ZnO 12 samples are the most defective) and the maximum of the PL emission in the visible range is located at 630 nm for these samples, which is attributed to the presence of Au impurities. The presence of Au has a clear effect in boosting the responsiveness towards ethanol for these two samples. Noble metal clusters such as Au NPs have been reported effective at the chemical sensitization of metal oxides [22], as they promote an increased number of oxygen surface species at the metal oxide host. This effect also explains why ZnO 6 and ZnO 12 samples retain responsiveness towards ethanol, even when in the presence of ambient moisture, which was not the case for ZnO 3 samples. The responsiveness towards NO_2 under dry conditions is clearly dominated by the presence of defects in the ZnO NWs. This explains why the more defective ZnO 12 samples, followed by ZnO 3 samples and the less defective ZnO 6 sample show decreasing responsiveness to NO_2, respectively. Besides the number of defects, the presence of Au NPs has a detrimental effect in the detection of NO_2 in the presence of ambient moisture, as ZnO 3 becomes the most NO_2 responsive material when under humid conditions. Au NPs in ZnO 6 and ZnO 12 samples may favour breaking the water molecule and the formation of radicals that spill over the metal oxide surface limiting the number of available sites for NO_2.

5. Conclusions

ZnO NWs were successfully synthetized through CVD (VLS growth mechanism) after employing different thicknesses (3, 6 and 12 nm) for the Au catalyst layer deposited by sputtering. The thickness of the catalyst layer has a high influence in the number of defects in the resulting ZnO NWs and in the presence/absence of Au impurities. ZnO 6 is the material with fewer defects and ZnO 3 is the material in which surface Au impurities are not detected in a chemical mapping. The direct growth of the gas sensitive nanomaterials onto the application substrates results in increased sensitivity and stability. ZnO NWs grow with no particular orientation in the form of disordered mats. ZnO NWs show high sensitivity towards NO_2 at ppb levels when operated at 250 °C. This sensitivity could be related to these materials having a significant number of defects, as revealed by PL analysis. While a higher number of defects (surface or/and bulk) seems favourable for the detection of NO_2, the presence of Au impurities (e.g. in the form of Au NPs at the surface of ZnO NWs) has been found detrimental when in the presence of ambient moisture. On the other hand, the presence of Au NPs helps enhance ethanol detection, possibly by assisting in the catalytic decomposition of the ethanol molecule or by increasing the number of adsorbed oxygen species at ZnO wires. However, this should be confirmed with further studies. Given the fact that the ZnO 3 samples retain their responsiveness towards NO_2 in the presence of ambient moisture while they show no response to ethanol, this makes ZnO 3 a potentially suitable material for detecting NO_2 in atmospheres where ethanol could be an interfering species.

CRediT authorship contribution statement

Eric Navarrete: Investigation, Formal analysis, Data curation, Writing – original draft. **Fran Güell:** Funding acquisition, Investigation, Formal analysis, Writing – editing & review. **Paulina R. Martínez-Alanis:** Investigation, Formal analysis, Writing – editing & review. **Eduard Llobet:** Funding acquisition, Conceptualization, Supervision, Writing – editing & review.

Funding

This work has received funding from the European Union's Horizon 2020 research and innovation program under the Marie-Sklowdoska-Curie, European Commission Grant agreement 823895. Funded in part by MINECO and FEDER via Grant no. RTI2018-101580-B-I00, by AGAUR under Grant 2017SGR 418. E.N. gratefully acknowledges a doctoral fellowship from MINECO Grant no. BES-2016-076582. E.L. is supported by the Catalan institution for Research and Advanced Studies via the 2018 Edition of the ICREA Academia Award. P.R.M-A. acknowledges the Programa Ajut a la Recerca Transversal de l'IN2UB 2018 for financial support.

Author Contributions

Conceptualization, **F.G. and E.L.**; Methodology, **E.N. and P.R.N.**; Formal analysis, **E.N. and P.R.M-A.**; Investigation, **E.N. and P.R.M-A.**; Data curation, **E.N.** Writing – original draft, **E.N.**; Writing – review & editing, **P.R.M-A., F.G. and E.L.**; Supervision, **F.G. and E.L.**; Funding acquisition, **F.G. and E.L.** All authors have read and agreed to the published version of the manuscript.

Declaration of Competing Interest

The authors declare that they have no known competing financial interests or personal relationships that could have appeared to influence the work reported in this paper.

Appendix A. Supplementary material

Supplementary data associated with this article can be found in the online version at doi:10.1016/j.jallcom.2021.161923.

References

[1] H. Morkoç, Ü. Özgür, Ed., Wiley-VCH, Weinheim, Germany, 2009.
[2] H.Z. Wu, K.M. He, D.J. Qiu, D.M. Huang, J. Cryst. Growth 217 (1) (2000) 131–137.
[3] D.R. Sahu, Mater. Sci. Eng. B Solid-State Mater. Adv. Technol. 171 (1–3) (2010) 99–103.
[4] N. Ito, Y. Sato, P.K. Song, A. Kaijio, K. Inoue, Y. Shigesato, Thin Solid Films 496 (1) (2006) 99–103.
[5] R. Macaluso, C. Calì, R. Butté, S. Nicolay, E. Feltin, D. Martin, N. Grandjean, Thin Solid Films 539 (2013) 55–59.
[6] L. Znaidi, Mater. Sci. Eng. B Solid-State Mater. Adv. Technol. 174 (1–3) (2010) 18–30.
[7] E.G. Barbagiovanni, V. Strano, G. Franzò, I. Crupi, S. Mirabella, Appl. Phys. Lett. 106 (9) (2015) 3–7.
[8] F. Caruso, M. Mosca, R. Macaluso, C. Cali, E. Feltin, in: Proceedings of the IEEE-NANO 2015 – 15th Int. Conf. Nanotechnol, 2015, pp. 1012–14.
[9] Z.L. Wang, J. Phys. Condens. Matter 16 (2004) 25.
[10] F.M. Simanjuntak, D. Panda, K.H. Wei, T.Y. Tseng, Nanoscale Res. Lett. 11 (2016) 1.
[11] R. Macaluso, M. Mosca, V. Costanza, A. D'Angelo, G. Lullo, F. Caruso, C. Calì, F. Di Franco, M. Santamaria, F. Di Quarto, Electron. Lett. 50 (4) (2014) 262–263.
[12] A. Moezzi, A.M. McDonagh, M.B. Cortie, Chem. Eng. J. 185–186 (2012) 1–22.
[13] A. Boughelouta, N. Zebbar, R. Macaluso, Z. Zohour, A. Bensouilah, A. Zaffora, M.S. Aida, M. Kechouan, M. Trari, Optik 174 (August) (2018) 77–85.
[14] A. Boughelout, R. Macaluso, M. Kechouane, M. Trari, React. Kinet. Mech. Catal. 129 (2) (2020) 1115–1130.
[15] Z.L. Wang, Springer-Verlag, Berlin, Heidelberg, DEU, 2012.
[16] R. Macaluso, G. Lullo, I. Crupi, D. Sciré, F. Caruso, E. Feltin, M. Mosca, Electronics 9 (2020) 6.
[17] R. Macaluso, G. Lullo, I. Crupi, F. Caruso, E. Feltin, M. Mosca, IEEE Trans. Electron Devices 66 (11) (2019) 4811–4816.
[18] M. Suchea, S. Christoulakis, K. Moschovis, N. Katsarakis, G. Kiriakidis, Thin Solid Films 515 (2) (2006) 551–554.
[19] Q. Wan, Q.H. Li, Y.J. Chen, T.H. Wang, Appl. Phys. Lett. 84 (18) (2004) 3654–3656.
[20] H. Okuma, T. Takahashi, M. Katsura, N. Ichinose, Toshiba Rev. (Int. Ed.) 118 (1978) 31–34.
[21] G. Heiland, Homogeneous semiconducting gas sensors, Sens. Actuators B-Chem. 2 (1981) 343–361.
[22] N. Yamazoe, Y. Kurokawa, T. Seiyama, Sens. Actuators B-Chem. 4 (1983) 283–289.

[23] B. Bott, T.A. Jones, B. Mann, Sens. Actuators B-Chem. 5 (1) (1984) 65–73.
[24] S. Saito, M. Miyayama, K. Koumoto, H. Yanagida, J. Am. Ceram. 68 (1985) 40–43.
[25] H. Nanto, T. Minami, S. Takata, J. Appl. Phys. 60 (2) (1986) 482–484.
[26] S.P.S. Arya, A. D'Amico, E. Verona, Thin Solid Films 157 (1) (1988) 169–174.
[27] J.X. Wang, X.W. Sun, Y. Yang, H. Huang, Y.C. Lee, O.K. Tan, L. Vayssieres, Nanotechnology 17 (19) (2006) 4995–4998.
[28] S. Roso, F. Güell, P.R. Martínez-Alanis, A. Urakawa, E. Llobet, Sens. Actuators B Chem. 230 (2016) 109–114.
[29] X. Zhou, A. Wang, Y. Wang, L. Bian, Z. Yang, Y. Bian, Y. Gong, X. Wu, N. Han, Y. Chen, ACS Sens. 3 (11) (2018) 2385–2393.
[30] Y. Li, S. Wang, P. Hao, J. Tian, H. Cui, X. Wang, Sens. Actuators B-Chem. 273 (June) (2018) 751–759.
[31] I. Paulowicz, V. Postica, O. Lupan, N. Wolff, S. Shree, A. Cojocaru, M. Deng, Y. Mishra, K.I. Tiginyanu, L. Kienle, R. Adelung, Sens. Actuators B-Chem. 262 (2018) 425–435.
[32] C. Xiangfeng, J. Dongli, A.B. Djurišic, Y.H. Leung, Chem. Phys. Lett. 401 (4–6) (2005) 426–429.
[33] S. Agarwal, P. Rai, E. Navarrete, E. Llobet, F. Güell, M. Kumar, K. Awasthi, Sens. Actuators B-Chem. 292 (April) (2019) 24–31.
[34] J. Chang, M.Z. Ahmad, W. Wlodarski, E.R. Waclawik, Sensors 13 (7) (2013) 8445–8460.
[35] A. Bobkov, A. Varezhnikov, I. Plugin, F.S. Fedorov, V. Trouillet, U. Geckle, M. Sommer, V. Goffman, V. Moshnikov, V. Sysoev, Sensors 19 (19) (2019) 4265.
[36] Y. Li, S. Wang, P. Hao, J. Tian, H. Cui, X. Wang, Sens. Actuators B-Chem. 273 (June) (2018) 751–759.
[37] X. Wang, F. Sun, Y. Duan, Z. Yin, W. Luo, Y.A. Huang, J. Chen, J. Mater. Chem. C 3 (43) (2015) 11397–11405.
[38] H. Nanofibers, K. Lokesh, G. Kavitha, E. Manikandan, G.K. Mani, IEEE Sens. J. 16 (8) (2016) 2477–2483.
[39] J.H. Lee, J.Y. Kim, J.H. Kim, S.S. Kim, Sensors 19 (3) (2019) 726.
[40] X. Pan, X. Zhao, J. Chen, A. Bermak, Z. Fan, Sens. Actuators B-Chem. 206 (2015) 764–771.
[41] M. Tonezzer, T.T. Le Dang, N. Bazzanella, V.H. Nguyen, S. Iannotta, Sens. Actuators B-Chem. 220 (2015) 1152–1160.
[42] M.N. Cardoza-Contreras, J.M. Romo-Herrera, L.A. Ríos, R. García-Gutiérrez, T.A. Zepeda, O.E. Contreras, Sensors 15 (12) (2015) 30539–30544.
[43] C.H. Kwak, H.S. Woo, F. Abdel-Hady, A.A. Wazzan, J.H. Lee, Sens. Actuators B-Chem. 223 (2016) 527–534.
[44] S. Vallejos, N. Pizúrová, I. Gràcia, C. Sotelo-Vazquez, J. Čechal, C. Blackman, I. Parkin, C. Cané, ACS Appl. Mater. Interfaces 8 (48) (2016) 33335–33342.
[45] M. Amin, U. Manzoor, M. Islam, A.S. Bhatti, N.A. Shah, Sensors 12 (10) (2012) 13842–13851.
[46] S. Öztürk, N. Kilinç, N. Taşaltin, Z.Z. Öztürk, Thin Solid Films 520 (3) (2011) 932–938.
[47] S. Bai, X. Liu, D. Li, S. Chen, R. Luo, A. Chen, Sens. Actuators B-Chem. 153 (1) (2011) 110–116.
[48] P.S. Cho, K.W. Kim, J.H. Lee, J. Electroceram. 17 (2–4) (2006) 975–978.
[49] T. Gao, T.H. Wang, Appl. Phys. A Mater. Sci. Process. 80 (7) (2005) 1451–1454.
[50] S. Tian, F. Yang, D. Zeng, C. Xie, J. Phys. Chem. C 116 (19) (2012) 10586–10591.
[51] F. Güell, A. Cabot, S. Claramunt, A.O. Moghaddam, P.R. Martínez-Alanis, Nanomaterials 11 (2021) 870.
[52] F. Güell, P.R. Martínez-Alanis, J. Lumin. 210 (2019) 128–134.
[53] F. Güell, P.R. Martínez-Alanis, S. Roso, C.I. Salas-Pérez, M.F. García-Sánchez, G. Santana, B.M. Monroy, Mat. Res. Exp. 3 (065013) (2016) 1–12.
[54] D.S. Kim, R. Scholz, U. Gösele, M. Zacharias, Small 4 (10) (2008) 1615–1619.
[55] V.V. Petrov, E.M. Bayan, S.A. Khubezhov, Y.N. Varzarev, M.G. Volkova, Chemosensors 8 (2) (2020) 40.
[56] D.V. Yakimchuk, V.D. Bundyukova, J. Ustarroz, H. Terryn, K. Baert, A.L. Kozlovskiy, M.V. Zdorovets, S.A. Khubezhov, A.V. Trukhanov, S.V. Trukhanov, L.V. Panina, G.M. Arzumanyan, K.Z. Mamatkulov, D.I. Tishkevich, E.Y. Kaniukov, V. Sivakov, Sensors 20 (16) (2020) 4397.
[57] P. Kundu, N. Singhania, G. Madrasb, N. Ravishankar, Dalton Trans. 41 (2012) 8762–8766.
[58] F. Güell, J.O. Ossó, A.R. Goñi, A. Cornet, J.R. Morante, Nanotechnology 20 (31) (2009) 315701.
[59] J.S. Reparaz, F. Güell, M.R. Wagner, G. Callsen, R. Kirste, S. Claramunt, J.R. Morante, A. Hoffmann, Appl. Phys. Lett. 97 (13) (2010) 133116.
[60] N.H. Alvi, K. ul Hasan, O. Nur, M. Willander, Nanoscale Res. Lett. 6 (1) (2011) 1–7.
[61] S. Pati, S.B. Majumder, P. Banerji, J. Alloy. Compd. 541 (2012) 376–379.
[62] L. Wu, Y. Wu, X. Pan, F. Kong, Opt. Mater. 28 (2006) 418–422.
[63] C.H. Ahn, Y.Y. Kim, D.C. Kim, S.K. Mohanta, H.K. Cho, J. Appl. Phys. 105 (2009) 013502.
[64] L. Cuia, H.-Y. Zhang, G.-G. Wang, F.-X. Yang, X.-P. Kuang, R. Sun, J.-C. Han, Appl. Surf. Sci. 258 (2012) 2479–2485.
[65] V. Kumar, H.C. Swart, O.M. Ntwaeaborwa, R.E. Kroon, J.J. Terblans, S.K.K. Shaat, A. Yousif, M.M. Duvenhage, Mater. Lett. 101 (2013) 57–60.
[66] D.E. Motaung, G.H. Mhlongo, S.S. Nkosi, G.F. Malgas, B.W. Mwakikunga, E. Coetsee, H.C. Swart, H.M.I. Abdallah, T. Moyo, S.S. Ray, ACS Appl. Mater. Interfaces 6 (2014) 8981–8995.
[67] H. Alnoor, C.O. Chey, G. Pozina, X. Liu, V. Khranovskyy, M. Willander, O. Nur, J. Appl. Phys. 19 (2015) 087180.
[68] A.N. Gruzintsev, V.T. Volkov, I.I. Khodos, T.V. Nikiforova, M.N. Koval'chuk, Russ. Microelectron. 31 (2002) 200–205.
[69] H. Liao, W. Wen, G.K.L. Wong, J. Opt. Soc. Am. B 23 (2006) 2518–2521.
[70] F. Güell, P.R. Martínez-Alanis, S. Khachadorian, J. Rubio-Garcia, A. Franke, A. Hoffmann, G. Santana, Phys. Stat. Sol. B 253 (2016) 883–888.
[71] M. Tonezzer, N.V. Hieu, Sens. Actuators B-Chem. 163 (2012) 146–152.
[72] N. Yamazoe, G. Sakai, K. Shimanoe, Catal. Surv. Asia 7 (2003) 63–75.
[73] A. Moumen, N. Kaur, N. Poli, D. Zappa, E. Comini, J. Nanomater. 10 (10) (2020) 1–16.
[74] S. Roso, C. Bittencourt, P. Umek, O. González, F. Güell, A. Urakawa, E. Llobet, J. Mater. Chem. C 4 (2016) 9418–9427.
[75] S. Roso, D. Degler, E. Llobet, N. Barsan, A. Urakawa, ACS Sens. 2 (2017) 1272–1277.